Superresolution 4π Raman microscopy

Alejandro Diaz Tormo,[1,*] Dmitry Khalenkow,[2] Kumar Saurav,[1] Andre G. Skirtach,[2] and Nicolas Le Thomas[1]

[1]Photonics Research Group, Department of Information Technology, Ghent University-imec & Center for Nano- and Biophotonics, Ghent University, Ghent, Belgium

[2]Department of Molecular Biotechnology, Ghent University, Ghent, Belgium

*Corresponding author: alejandro.diaztormo@ugent.be

Received 1 September 2017; accepted 26 September 2017; posted 2 October 2017 (Doc. ID 306261); published 24 October 2017

The advent of 4π microscopy broke the conventional optical resolution limit in the axial direction of the microscope. In combination with fluorescence microscopy, it broadened the knowledge of cell biology at the expense of perturbing the samples with extrinsic fluorescent labels. In contrast, Raman microscopy acquires the molecular fingerprint of the sample without the need of extrinsic labels, and therefore improving its resolution can make an even greater impact. Here, we take advantage of the improved axial resolution of a 4π configuration to form a 4π Raman microscope. With this microscope, we independently and simultaneously analyzed different nanolayers in a multilayer stack. We identified their chemical composition and retrieved their relative subwavelength optical separation with a precision of 6 nm. © 2017 Optical Society of America

OCIS codes: (180.1790) Confocal microscopy; (170.0110) Imaging systems; (310.0310) Thin films; (120.2130) Ellipsometry and polarimetry; (180.5655) Raman microscopy; (110.1080) Active or adaptive optics.

https://doi.org/10.1364/OL.42.004410

Fluorescence nanoscopy [1,2] has pushed the resolution boundaries of biological imaging. Raman microscopy [3,4], with the fundamental advantage of being label-free, is certainly following the same direction, and new research avenues are already being explored [5–8]. Through the study of a nanolayer stack, we show that using a 4π configuration [9] to Raman microscopy has a great potential to help in this quest. Nanolayers have attracted increasing interest across a wide diversity of fields, such as optics [10], energy storage [11], biology [12], and pharmacology [13]. They are typically characterized via ellipsometry, electron microscopy, or x-rays; however, these techniques share a common limitation: data from complex stacks of nanolayers become increasingly difficult to interpret. 4π Raman microscopy allows for determination of the macrostructure and microstructure, optical properties, and chemical composition of each nanolayer separately at the same time, which is hardly feasible with other techniques. In addition, it is noninvasive and probes diffraction limited areas, and complex model fittings are needless.

Here, we developed a 4π configuration with a Raman microscope in order to obtain a point-spread function that depends on the phase difference between opposing pump beams. We can phase shift one of the beams to vertically scan the sample but without actually moving it, as it would be done in conventional Raman microscopy. In addition, we obtained theoretically twice the Raman signal intensity of standard spontaneous Raman microscopy.

The working principle of 4π microscopy is depicted in Fig. 1 and compared to conventional microscopy. In the latter, a single objective lens normally provides better transversal resolution (in the image plane) than axial resolution (in the propagation direction). The stack of nanolayers in Fig. 1(a) would normally be probed with a typical intensity point-spread function represented in Fig. 1(b). In 4π microscopy, two

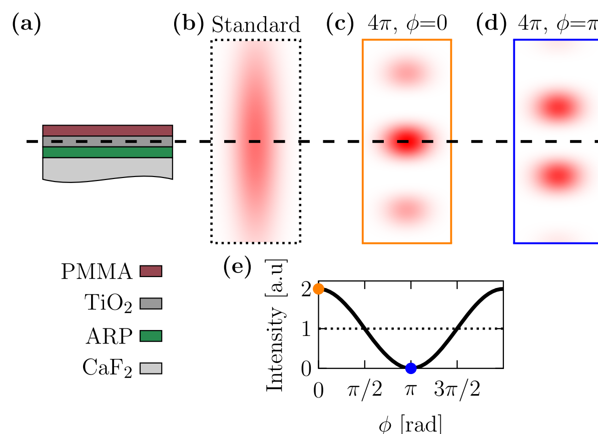

Fig. 1. Working principle of the 4π microscope. Drawings not to scale. Only the pump beam is shown. (a) Sample schematic. The thickness of the layers are: PMMA 43 nm, TiO_2 23 nm, ARP 65 nm, and the CaF_2 substrate 1 mm. (b) Standard confocal intensity point spread function. Note that it is independent of the phase, since it is produced by just one beam. (c) and (d) 4π point spread function showing the fringe pattern when both beams are in phase and out of phase, respectively. (e) Intensity at the dashed line versus relative phase between counter-propagating beams ϕ.

counter-propagating coherent beams produce an interference pattern in the common focal spot, as shown in Figs. 1(c) and 1(d), reducing the effective illuminated volume and improving the axial resolution up to sevenfold [14]. The pump intensity at each nanolayer follows a sinusoidal curve when the relative phase between exciting beams ϕ is varied (see Fig. 1[e]). Importantly, depending on their position, their sinusoidal responses are shifted along the phase axis with respect to each other. Since these responses are obtained from independent fingerprints, we can measure their positions with much higher accuracy than the diffraction limit allows. We shall refer to ϕ as "nominal phase" henceforth.

In order to manipulate the position of the fringe pattern at the sample plane, we developed the interferometer sketched in Fig. 2. It was tailored to control and measure the relative phase between both pump beams at the sample plane. Additionally, it was used to compensate for the phase noise in the system introduced by the fibers in the interferometer [15]. There are four beams traveling throughout the interferometer (red arrows), two transmitted and two reflected beams from the semitransparent sample. The isolator in the bottom arm blocks two of them (red dashed arrows), and thus we record only a two-beam interferogram. The photodetector is sensitive to the cos ϕ term generated by the interference between the remaining two beams (red solid arrows). These beams co-propagate over the same fiber, and therefore they will suffer the same phase shift in their path toward the detector. In this way, the phase difference at the sample plane can be retrieved with the detector being at a completely different plane.

In the experiments, we used a commercial confocal Raman microscope (WITec Alpha300R+) equipped with a UHTS 300 spectrometer and a –70°C cooled CCD camera (ANDOR iDus 401 BR-DD) to record the Raman spectra. We collected the Raman signal solely from the top objective, and each spectrum acquisition took 170 s. The objective lenses used in the top and bottom sides of the sample have a numerical aperture of 0.9 and 0.5, respectively. A single-mode laser

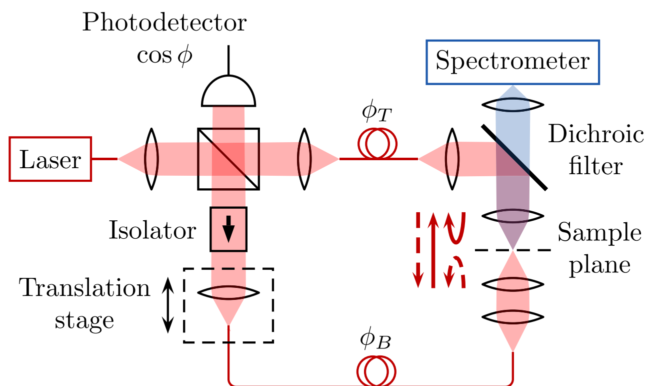

Fig. 2. Schematic of the optical setup. Four optical beams are present in the interferometer. Two of them are blocked by the isolator (dashed red arrows). The remaining two beams interfere, producing the term cos ϕ at the photodetector, where ϕ is the difference between the phase shift induced by the bottom and top fibers, $\phi = \phi_B - \phi_T$. Red paths relate to the pump, whereas blue indicates Raman signal. The photodetector signal is sent to a feedback loop that controls the translation stage to stabilize the interferogram.

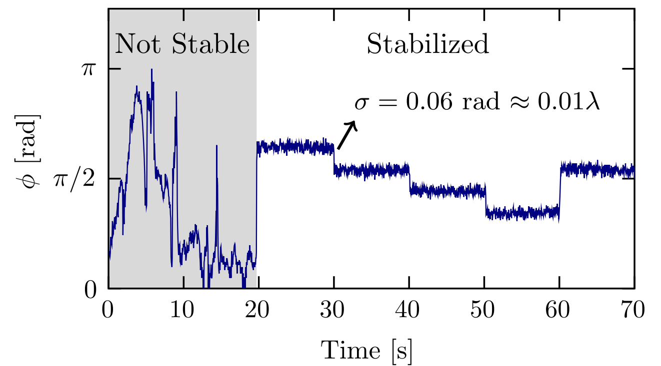

Fig. 3. Demonstration of the phase control and stabilization. Shadowed area indicates the environmental phase noise in the free-running system.

diode (Toptica XTRA II) with wavelength $\lambda = 785$ nm was used as the pump.

The control over the nominal phase is demonstrated in Fig. 3. The parameters of the proportional–integral–derivative (PID) controller, which is part of the feedback loop, were adjusted to set the desired nominal phase. The feedback loop control was turned on after 20 s. In the stabilized regime, we set the nominal phase to a different value every 10 s. The standard deviation of the different steps was approximately $\sigma = 0.06$ rad, or equivalently 0.01λ.

The translation stage consisted of a piezoelectric actuator that moved one of the collimating lens present in the interferometer with its corresponding fiber attached. Despite having a cut-off frequency of 300 Hz (relatively low compared to similar studies [16]) it significantly reduced the environmental phase noise present in our setup as shown in Fig. 3.

To highlight the potential of 4π Raman microscopy, we analyzed the multilayer sample depicted in Fig. 1(a) consisting of three stacked nanolayers on top of a 1 mm thick CaF_2 substrate. We selected a Raman grade CaF_2 substrate because of its low fluorescence background. The layers from top to bottom are polymethyl methacrylate (PMMA), amorphous titanium oxide (TiO_2), and e-beam resist (ARP). The PMMA and ARP layers were spin-coated, whereas the TiO_2 was deposited via sputtering. The molecular fingerprint of the multilayer stack is indicated in Fig. 4(a). The molecules from each layer can be identified by their unique signatures. In particular, TiO_2 presents a broader fingerprint than the other components, from

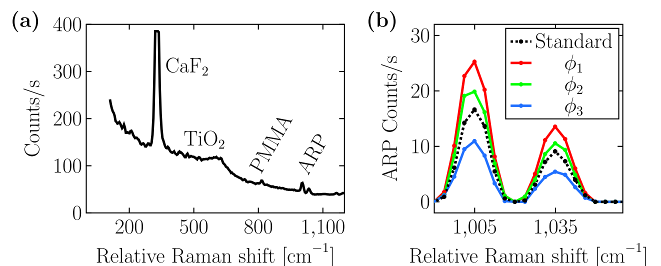

Fig. 4. 4π Raman spectra. (a) Full Raman spectrum showing the different material contributions. (b) Zoom-in of the ARP peaks with the background removed. Dashed black indicates the standard confocal spectrum. Spectra at different nominal phases are color coded.

0 to 630 cm^{-1}. Overall, their main spectral features are separated, which allows them to be studied independently. In Fig. 4(b), the ARP Raman peaks are plotted for the standard measurement and for different nominal phases, demonstrating a precise phase control of the fringe pattern at the sample plane. The standard measurement is done under the same conditions as the 4π measurements except that it is incoherent, i.e., it is taken under intentional high phase noise conditions. During this measurement, the nominal phase changed randomly over the full 2π range much more rapidly than the measurement acquisition time.

In Fig. 5, the intensity of the highest ARP and PMMA Raman peaks, as well as the intensity of the broad TiO_2 spectrum, are plotted for different nominal phases ϕ. Since the vertical axis is normalized with respect to the standard measurement, it represents the enhancement factor. The data are fitted to a cosine curve with a unity offset to obtain amplitude and phase shift. Each response has a different phase shift. In particular, the response corresponding to TiO_2 lies in the middle of the other two, in line with the layer distribution.

Instead of the expected enhancement factor of 2, we recorded a factor of 1.41 for ARP and PMMA, and slightly lower for TiO_2. This factor is directly linked to the contrast of the interference pattern at the sample plane, which can be reduced for many reasons. The width of the layers themselves partially explains the reduced experimental contrast. As a reference, the particular case of a 64.5 nm ARP layer with refractive index $n_{\mathrm{ARP}} = 1.56$ yields a theoretical contrast of 1.89. The other relevant factor reducing the contrast is the aberration suffered by the bottom beam due to the 1 mm thick CaF_2 substrate.

The phase shift $\theta = 2.3 \pm 0.1$ rad between the ARP and PMMA interferograms in Fig. 5 is related to the optical length between these layers. If both Raman signals came exactly from the same plane, the cosine fits would overlap. For such subwavelength layer thicknesses, the strongest Raman peaks are collected when a fringe maximum sits at their barycenters. Consequently, the phase shift stems from the different optical lengths the pump has to travel to reach the layer barycenters. Based on the phase shift θ, we determined an optical length between ARP and PMMA layers of 141 ± 6 nm.

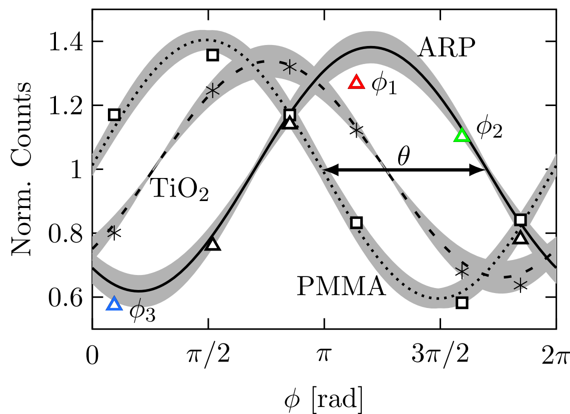

Fig. 5. Response of the ARP, PMMA, and TiO_2 layers versus nominal phase. They are normalized with respect to the standard response and fitted to a cosine curve. Colors indicate the same data as in Fig. 4(b). Triangles and straight line relate to the ARP experimental data points and their fit, respectively. The process is replicated for PMMA yielding the squares and dotted curve, as well as for TiO_2 with stars and dashed curve. θ is the phase shift between the ARP and PMMA interferograms. The measurements are repeated five times for error analysis. Shadowed areas indicate the standard deviation of the fittings, which results in an optical path length resolution of 6 nm.

For comparison purposes, we also characterized the sample by ellipsometry [17], which uses fitting models to extract the sample information. However, due to the high number of fitting parameters, i.e., refractive indices and thicknesses of all the layers, the result was inconsistent. For that reason, we fabricated a dedicated single-layer sample for each material of the stack and determined their thicknesses. The fabrication process of these single-layer samples was the same as in the multilayer stack. The thicknesses obtained were 43 nm, 23 nm, and 65 nm for PMMA, TiO_2, and ARP, respectively. The refractive indices were $n_{\mathrm{PMMA}} = 1.48$, $n_{\mathrm{TiO_2}} = 2.2$, and $n_{\mathrm{ARP}} = 1.56$. From these values, we could calculate the total optical path separation between the centers of the PMMA and ARP layers. We obtained a value of 131 ± 8 nm, in line with the 4π Raman microscopy result.

To conclude, we have demonstrated 4π Raman microscopy and how it can be used to characterize a nanolayer stack. We could enhance its Raman signal by a factor of 1.41 compared to standard confocal microscopy and at the same time obtain a superresolution of 6 nm with regard to the optical length. The fundamental advantage of this technique is that it provides the Raman fingerprint of the sample under study and therefore is suited to simultaneously study several layers.

The microscope described here is a tool to measure the thickness, refractive index, and/or position of multiple layers within a layer stack with deep subwavelength accuracy. As with other instruments [18], we could extract the refractive index and/or physical thickness from our optical length data by measuring the sample under various angles of incidence or pump wavelengths. Local changes in the material structure can also be detected from diffraction limited areas since they are reflected on the Raman fingerprint.

We expect 4π Raman microscopy to be advantageous—in terms of signal collection and resolution—for thin-film characterization, biochemical imaging studies, and material sciences, among others.

Funding. Bijzonder Onderzoeksfonds (BOF) (24J201400010); ERA-Net RUS Plus project 'Intelbiocomp'

Acknowledgment. The authors thank S. Verstuyft for helping with the ellipsometry measurements.

REFERENCES

1. S. W. Hell, R. Schmidt, and A. Egner, Nat. Photonics **3**, 381 (2009).
2. S. W. Hell, Science **316**, 1153 (2007).
3. C. Krafft and J. Popp, Anal. Bioanal. Chem. **407**, 699 (2015).
4. A. Yashchenok, A. Masic, D. Gorin, B. S. Shim, N. A. Kotov, P. Fratzl, H. Möhwald, and A. Skirtach, Small **9**, 351 (2013).
5. K. Watanabe, A. F. Palonpon, N. I. Smith, L. Chiu, A. Kasai, H. Hashimoto, S. Kawata, and K. Fujita, Nat. Commun. **6**, 10095 (2015).
6. C. Neumann, S. Reichardt, P. Venezuela, M. Drögeler, L. Banszerus, M. Schmitz, K. Watanabe, T. Taniguchi, F. Mauri, B. Beschoten, S. V. Rotkin, and C. Stampfer, Nat. Commun. **6**, 8429 (2015).
7. W. R. Silva, C. T. Graefe, and R. R. Frontiera, ACS Photon. **3**, 79 (2015).

8. L. Langelüddecke, P. Singh, and V. Deckert, Appl. Spectrosc. **69**, 1357 (2015).
9. S. W. Hell, E. H. K. Stelzer, S. Lindek, and C. Cremer, Opt. Lett. **19**, 222 (1994).
10. S. Yoo, T. Gwon, T. Eom, S. Kim, and C. S. Hwang, ACS Photon. **3**, 1265 (2016).
11. J. Liu, S. Tang, Y. Lu, G. Cai, S. Liang, W. Wang, and X. Chen, Energy Environ. Sci. **6**, 2691 (2013).
12. Y. Okamoto, T. Ikeda, K. Suga, and H. Umakoshi, Chem. Lett. **45**, 622 (2016).
13. M. Choi, K. Kim, J. Heo, H. Jeong, S. Y. Kim, and J. Hong, Sci. Rep. **5**, 17631 (2015).
14. S. W. Hell and E. H. K. Stelzer, J. Opt. Soc. Am. A **9**, 2159 (1992).
15. R. E. Bartolo, A. B. Tveten, and A. Dandridge, IEEE J. Quantum Electron. **48**, 720 (2012).
16. S. B. Cho and T. G. Noh, Opt. Express **17**, 19027 (2009).
17. A. Rothen, Rev. Sci. Instrum. **16**, 26 (1945).
18. J. Schilling, K. Sengupta, S. Goennenwein, A. R. Bausch, and E. Sackmann, Phys. Rev. E **69**, 021901 (2004).

157.193.240.1 {ts '2017-10-23 03:49:16'}